Time-lapse geophysical imaging of soil moisture dynamics in tropical deltaic soils: An aid to interpreting hydrological and geochemical processes

D. A. Robinson,[1,2] I. Lebron,[1,2] B. Kocar,[3] K. Phan,[4] M. Sampson,[4] N. Crook,[1] and S. Fendorf[3]

Received 9 March 2008; revised 8 January 2009; accepted 19 January 2009; published 26 March 2009.

[1] A fundamental, and often intriguing question, in hydrology is ''where does the water go?'' This becomes particularly difficult to observe when water arrives at the ground surface and infiltrates into soils. The development of rapid, campaign-style imaging methods that do not need to be left in situ are therefore of great interest in tracking subsurface hydrological redistribution. We present a novel geophysical imaging approach identifying spatiotemporal variation consistent with soil water redistribution in a tropical deltaic soil. The intention is to provide additional insight into spatiotemporal soil hydrological/biogeochemical processes. The bulk soil electrical conductivity response (EC_a) is primarily controlled by the clay content and type, the ions retained in the soil solution (EC_e), and the soil water content (θ). Clay content can be assumed to be temporally static, whereas θ and EC_e are temporally dynamic. By imaging over time, we can attempt to tease apart these contributing factors. In nonsaline soils θ is the major contributor to temporal changes in EC_a. By exploiting an intensive rainfall event (75 mm), with time series spatial EC_a measurements, before and after the event, we were able to identify zones of water depletion and accumulation and to provide an indication of the time required for the soil to return to its prior state. In addition, locations with more clay and salts were identified through response surface-directed soil sampling. We found important spatiotemporal variation across the level 4 ha field site that from visual inspection appeared uniform.

Citation: Robinson, D. A., I. Lebron, B. Kocar, K. Phan, M. Sampson, N. Crook, and S. Fendorf (2009), Time-lapse geophysical imaging of soil moisture dynamics in tropical deltaic soils: An aid to interpreting hydrological and geochemical processes, *Water Resour. Res.*, *45*, W00D32, doi:10.1029/2008WR006984.

1. Introduction

[2] Where does the water go? This is a fundamental question within hydrology, particularly in the context of the infiltration and redistribution of water in soils following precipitation. Once water enters the soil there is a severe limitation in our ability to track and visualize where, and how, water moves. This is particularly difficult in developing countries where sensors and monitoring equipment can rarely be left in place. Therefore, the development of rapid, campaign style, imaging methods that do not need to be left in situ are of great interest to track subsurface hydrological processes.

[3] Hydrologists have been inventive in developing models and methods of predicting the movement of water in the subsurface. Fortunately, water moves according to potential gradients, mainly gravitational and matrix forces. This has allowed the development of theories and models to describe infiltration [*Philip*, 1969] and soil water dynamics [*Daly and Porporato*, 2005]. The development of advanced sensor technologies for determining soil moisture [*Robinson et al.*, 2008a; *Huisman et al.*, 2003] and soil water potential at a point has allowed the testing of 1-D infiltration theory in both the laboratory and field [*Si and Kachanoski*, 2000; *Noborio et al.*, 1996]. However, even with these advances, there remain significant gaps in our understanding and ability to measure infiltration and redistribution processes at the field scale. This is especially true in developing countries where monitoring equipment is vulnerable. Even with the collection of point data, the problem is often encountered, that the scale of the point data is incommensurate with hydrological process models [*Beven*, 2001]. This results in a lack of good quality hydrological process data, especially for the intermediate scales [*Western et al.*, 2002].

[4] The flow of water through a 3-D landscape presents a much greater challenge. As topography becomes steeper so gravity dominates the movement of water. Digital elevation models (DEMs) have been used to determine flow paths and can be combined with hydrological models to estimate the

[1]Department of Geophysics, Stanford University, Stanford, California, USA.
[2]Now at Department of Food Production, University of the West Indies, Saint Augustine, Trinidad and Tobago.
[3]Department of Environmental Earth System Science, Stanford University, Stanford, California, USA.
[4]Resource Development International Cambodia, Phnom Penh, Cambodia.

0043-1397/09/2008WR006984$09.00

saturation index across the landscape [*Lane et al.*, 2004], but essentially remains a black box. A major limitation to advancing our understanding of subsurface flow processes is the lack of spatial data to test models, many of which have increased in complexity, but offer a range of non-unique results [*Beven*, 2001]. One measurement method that has proved particularly valuable, and continues to develop, is the use of tracers. This ranges from the use of dyes [*Flury and Wai*, 2003] to the measurement of isotopes [*Clark and Fritz*, 1997]. However, dyes are limited in subsurface applications to small areas and require destructive sampling. Other tracers, including chemical tracers such as chloride and bromide, and isotopic tracers can confirm the arrival time of water and with sampling via wells or destructively can be used to obtain a snapshot of the spatial pattern of a hydrological process [*Flury and Wai*, 2003, and references therein]. However, none of these methods provide an image of hydrological processes at the field scale, all of these techniques are either destructive or expensive, requiring extensive well sampling and chemical analysis to try and build up a spatial picture.

[5] Some may question the need for spatial imaging; however, in interdisciplinary studies where hydrology is a key control on biogeochemical processes, images, from which hydrological processes can be inferred, or the spatial extent of processes delineated, are invaluable in planning and interpreting field-scale research. Our rationale for developing a more advanced soil hydrological imaging method is to fill this need, particularly for biogeochemical studies, to identify and delimit spatial zones of soil moisture accumulation and depletion, and identify areas with the most obvious ''changes'' occurring. This methodology could be applied to the study of many soil processes including, pesticide movement or contaminant flow; however, our particular interest in Cambodia is to understand processes that govern the release of arsenic [As] in soils to groundwater.

[6] In southeast Asia contamination of groundwater by [As] has become a major humanitarian disaster with millions of contaminated drinking water wells [*Ahmed et al.*, 2006]. A range of processes have been postulated for the release (desorption) of [As] from the solids into the pore water; the onset of reducing conditions and ensuing reductive dissolution of [As]-bearing Fe (hydr)oxides is generally ascribed as the dominant mechanism [*Ahmed et al.*, 2004; *deLemos et al.*, 2006; *McArthur et al.*, 2001]. Organic carbon, transported from the surface [*Harvey et al.*, 2002], and more recently, soil and near-surface sediment redox processes have been identified as contributing mechanisms of [As] release to groundwater [*Polizzotto et al.*, 2008, 2005]. The purpose of this paper is not to enter into this debate about the source of [As], but to assist the biogeochemist in identifying potential zones of hydrological/biogeochemical change in soils, particularly soil moisture accumulation and depletion across a 4 ha deltaic field site. It must be remembered that in developing countries it is particularly difficult to obtain monitoring data because of difficulty with securing equipment. The development of rapid, campaign-style imaging methods that do not need to be left in situ in the field is of great interest for this style of research.

[7] The aim of the work was to observe hydrological processes by obtaining spatial images in time series that could be used to interpret hydrological processes across the field site, so as to understand spatial patterns in behavior. In particular to provide qualitative answers to the following questions, which are often of interest at many field sites.

[8] 1. In which area of the field site is drainage and change in conditions most apparent?

[9] 2. Following a precipitation event which locations are wettest and then return to prerainfall conditions most quickly, and how long does this take?

[10] 3. Where are the locations where clay is most likely to have accumulated?

[11] 4. Are there locations where soluble salts build up?

[12] The answers to these questions may help inform researchers as to how representative chosen sampling locations are, or may be used to guide soil sampling. From the biogeochemical view point, knowing where water depletes or accumulates gives some indication of likely redox conditions. Knowing the locations with more clay is important as greater biogeochemical reactive surface area becomes available; and identifying locations with more soluble salts is useful as adsorbed species may be released because of mass action. At this stage in the research the intention is to provide qualitative answers. As the research progresses the plan is to try to link hydrological and geophysical models to interpret the data more fully.

[13] Hydrogeology and the emerging discipline of hydrogeophysics [*Rubin and Hubbard*, 2005; *Robinson et al.*, 2008b] utilizes contrasts in earth physical properties, related to water, to provide what is at present semiquantitative data on the spatial patterns of hydrological processes. The advantage of the hydrogeophysical data is that often the data are noninvasive, and usually spatially exhaustive, allowing 2-D and 3-D [*Knight*, 2001] images to be obtained. The choice of hydrogeophysical approach depends on the hydrological problem, the earth properties, and the spatial and temporal resolution required. Applications of hydrogeophysics include determining the spatial pattern of soil moisture using ground penetrating radar (GPR) [*Huisman et al.*, 2003] and pollution plume detection and monitoring using electrical resistivity imaging (ERI). *Looms et al.* [2008] combined electrical resistivity and an electrical tracer to determine the important hydrological parameters such as flow velocity and longitudinal dispersivity of a pulse of water. In this research we focus on the use of electromagnetic induction (EMI), which has been used extensively to determine soil salinity [*Hendrickx et al.*, 1992; *Nettleton et al.*, 1994; *Bourgault et al.*, 1997; *Hendrickx and Kachanoski*, 2002; *Corwin and Lesch*, 2003; *Corwin and Lesch*, 2005], subsurface morphology [*James et al.*, 2003; *Comas et al.*, 2004], and texture [*Doolittle et al.*, 1994; *Triantafilis and Lesch*, 2005; *Jung et al.*, 2005], but has been used in a more limited way in hydrology with applications to determine soil moisture [*Kachanoski et al.*, 1988; *Sheets and Hendrickx*, 1995; *Kachanoski et al.*, 2002], and as a method of interpreting hillslope hydrological patterns [*Robinson et al.*, 2008c; *Sherlock and McDonnell*, 2003]. To our knowledge no attempt has been made to use the method as a combined spatiotemporal imaging tool to better define subsurface hydrological processes.

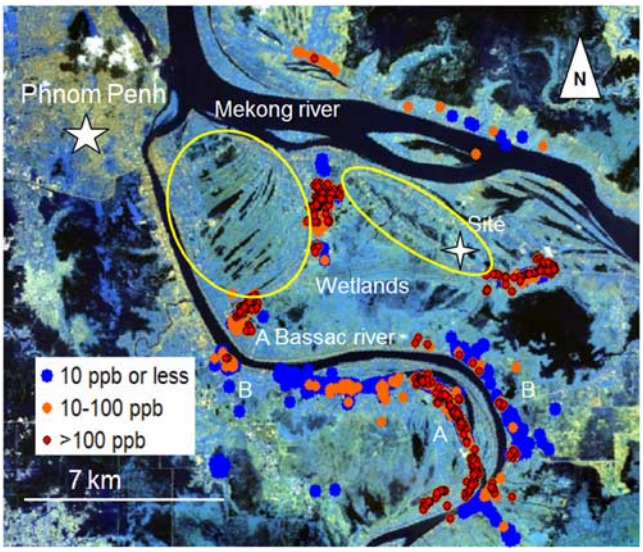

Figure 1. An NLT Landsat 7 pseudocolor image of the Cambodia capital Phnom Penh and the Kandal province region. The pseudocolor highlights the surface water as black, and most noticeably, the pseudocolor reveals the former channel structure and the pattern of abandoned oxbows (inside yellow circles), of which the field site (star marked "Site") is a part. The markers indicate well locations where water was tested for [As]. The World Health Organization limit for safe drinking water is 10 ppb, and many of the wells are over this limit.

[14] Our research, over the duration of a month, was used to obtain a series of images using multiple EMI surveys following a rainfall event. Inference of hydrological processes was based on changes in the soil electrical properties. The collection of multiple surveys in a time series allows for rank stability analysis of the data [*Vachaud et al.*, 1985], allowing us to locate areas where the bulk soil electrical conductivity (EC_a) is consistently higher or lower through time and observe change. Concurrently we performed a calibration with an EMI drainage experiment to determine the EC_a dependence on θ.

2. Theory of Electrical Measurements in Soils

2.1. Soil Electrical Properties

[15] The measurement of EC_a depends mostly on a combination of three distinct soil properties, θ, soil texture (clay %), and the soil solution extract electrical conductivity (EC_e) [*Friedman*, 2005]. The dependence of EC_a on EC_e has meant that EMI is the primary field technique used for identifying soil salinity [*Corwin and Lesch*, 2003]. EMI mapping protocols have been developed in this regard to provide quantitative estimates of soil salinity [*Corwin and Lesch*, 2005]. The dependence of EC_a on soil texture, θ and EC_e means that it can be difficult to determine, with certainty, which property is dominating the signal. Calibration methods using response surface and directed soil sampling have been developed for saline soils by *Lesch et al.* [1995a, 1995b] to interpret patterns using correlation and soil samples. In this work, in addition to using directed sampling, we also use a different approach, we assume that clay % is unchanging across the field site, i.e., it is temporally static, whereas θ and EC_e will be temporally dynamic. Because these soils are considered nonsaline, we assume that changes in θ will govern the EC_a response [*Mualem and Friedman*, 1991]. In addition it is important to note that increasing θ, EC_e and clay % all act to increase the EC_a response. This is advantageous in the study of [As] as all these factors may work together to enhanced [As] risk.

2.2. EMI Measurement Method

[16] Electromagnetic induction (EMI) is particularly suited to field-scale soil imaging work. The method is rapid, noninvasive and can be automated to collect georeferenced data. Unlike remote sensing methods, penetration depths into the soil vary from integrated averages of a few tens of centimeters to several meters depending on the transmitter and receiver spacing and orientation [*McNeill*, 1980; *Callegary et al.*, 2007]. EMI is becoming more widely used in soils research [*Robinson et al.*, 2008b]; however, it has not been widely adopted in process hydrology, or combined with biogeochemical studies, other than soil salinity research.

3. Materials and Methods

3.1. Site Description

[17] The study site was located in Kandal province southeast of Phnom Penh, Cambodia. It was situated between the Mekong and Bassac rivers (105.03963 latitude, 11.4996583 longitude) at an elevation of ~5 m above mean sea level (Figure 1). The region is characterized climatically by a wet and dry season. Following the snowmelt from the Himalaya, water levels rise in the rivers and the fields become flooded. With the onset of the dry season water levels decline, the fields emerge, and are used for agricultural production in the form of rice and vegetables. The area is full of small fields which are irrigated by hand using watering cans. Initially it was feared that this may influence EMI readings, but the irrigation is frequent and shallow, water penetrating no more than 5–10 cm, whereas the EMI in the vertical orientation responds to depths of 40–100 cm. The seasonal flooding flushes any salts from the soils that may build up from the previous growing season. This area is the remnant of an oxbow system, now abandoned with the new river course. The use of the NLT Landsat 7 pseudocolor image (Figure 1) indicates the structure of the abandoned oxbows, shown in the yellow circles. Many of these remain saturated throughout the dry season and provide a supply of water for irrigation.

[18] The Mekong delta floodplain is roughly 62,500 km^2 [*Nguyen et al.*, 2000] and the upper 7 to 20 m of sediment has been deposited as a prograding deltaic sequence in the past 6 ka [*Ta et al.*, 2002] following the most recent sea level highstand. Below surficial overbank clays, Holocene sediments representing delta progradation include organic-rich silts, sands, and clays; the gray sand sediments encompass the majority of wells within our field area and are those with which high dissolved [As] concentrations are typically associated [*Kocar et al.*, 2008]. Quaternary sediments underlay the Holocene sediments and were deposited during delta aggradation [*Ta et al.*, 2002]. The region of our site is characterized by elevated levees along river banks receding

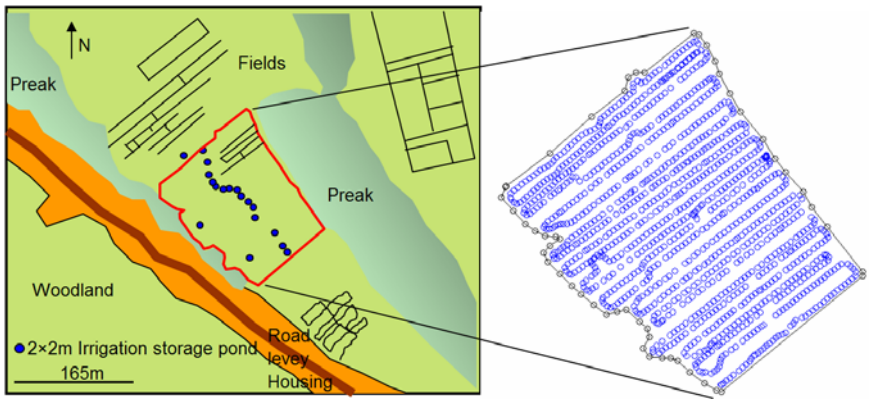

Figure 2. A detailed schematic of the field site showing its location nestled between two abandoned oxbows (Preak). The field site is entirely agricultural, with mostly vegetables and herbs being grown. To the right is the route taken while mapping the site, indicating the data collection density.

to a native wetland basin between the two rivers. The primary water-producing fine gray sand aquifer at our field site typically extends to >50 m depth and is overlain by a 3 to 20 m thick red and gray clay unit. We have installed a network of 80 wells and 10 surface water monitoring sites that are distributed throughout the basin area between the two rivers; [As] exists at concentrations above 100 μg/L nearly universally in the region across the flood plane except where local mixing with river water or flushing occurs [*Kocar et al.*, 2008]. The abandoned oxbow channel, which is the focus area for this study, has underlying [As] concentrations generally above 500 μg/L and hydrologic analysis reveals this area as a prime contributor to aquifer recharge [*Polizzotto et al.*, 2008; *Benner et al.*, 2008].

3.2. EMI Mapping and Calibration

[19] EMI soil imaging surveys were carried out between 15 March and 3 April 2007. A DUALEM-1S EMI sensor with a 1.1 m coil spacing was used during the work [*Abdu et al.*, 2007]. The sensor was carried at a height of about 25 cm above the soil surface. Using data collected from the EMI coils in the vertical orientation the instrument integrated most of its measurement over the top meter of soil [*Abdu et al.*, 2007], with the greatest sensitivity in the top half meter. The instrument was connected to a Trimble ProXT (Trimble Inc, San Jose, California) global positioning system (GPS) via a portable Allegro field computer (Juniper Systems Inc, Logan, Utah). Computer software allowed the simultaneous collection of the GPS location and the EMI signal. Measurements were made at 2 s intervals while traversing the field site at approximately 4 m intervals. The detailed map of the field site, situated between two inundated abandoned oxbows, is shown in Figure 2. A line of small $\sim 2 \times 2$ m ponds run along the center of the field; these are used to store irrigation water pumped from the abandoned oxbow lakes. One of the EMI route maps is shown on the right indicating the density of measurement over the site; approximately 1100 measurements were made for each image.

[20] The first EMI image was made on 15 March 2007 toward the end of the dry season. On the evening of 19–20 March a 75 mm rainfall event occurred. The next image was made on 20 March immediately following the rainfall event. Subsequent images were obtained on 21, 22, 23, 24, 26, and 30 March and 3 April. Soil temperatures were measured before and after measuring and did not change from 30°C, consistent with the tropical climate. Therefore, no temperature correction was needed for the data.

[21] Concurrently a calibration experiment was run to determine the EMI response to drainage of soil moisture. A 2×2 m bunded experimental plot was constructed at the location marked by the infiltration experiment in Figure 8. A ThetaProbe (DeltaT Devices, Burwell, Cambridge, United Kingdom) was buried in the soil at 40 cm. Bulk density measurements were made using soil cores and oven drying to determine the soil porosity ($\varphi = 0.41$). The EMI instrument was placed in the middle of the plot at a height similar to the mapping height by placing it on 2 bricks. Measurements of EC_a and θ were made when the soil was dry, before the rainfall event. After the rainfall event the experimental plot was flooded with water which was allowed to infiltrate into the soil over a 2 day period to ensure saturation. During the rainfall event the soil received 7.5 cm of water, we subsequently applied a further 50 cm of water to ensure saturation. Within 24 h the soil had reached a water content of 0.401 $m^3\ m^{-3}$, this water content was maintained during the addition of water over the following 24 h and considered to reflect the steady state water content. The value was also in close agreement to the porosity (0.41) determined from the bulk density samples. After 48 h the soil was allowed to drain naturally and EC_a and measurements of θ were made over the following 3 weeks.

3.3. Soil Sampling and Arsenic Measurements

[22] Soil samples were obtained as part of a larger sampling effort at nine locations across the field site. The sampling locations were identified using the EMI response surface and the directed soil sampling approach described by *Lesch et al.* [1995a, 1995b]. Soil samples were taken from 0 to 30 cm and from 30 to 60 cm depth. The samples were subsequently analyzed for θ by oven drying at 105°C. Subsamples were analyzed for soil texture using the sedimentation method for the particle size analysis [*Gee and Bauder*, 1986]. EC_e was determined by making a saturated paste and extracting the solution and measuring its electrical conductivity [*Rhoades*, 1982].

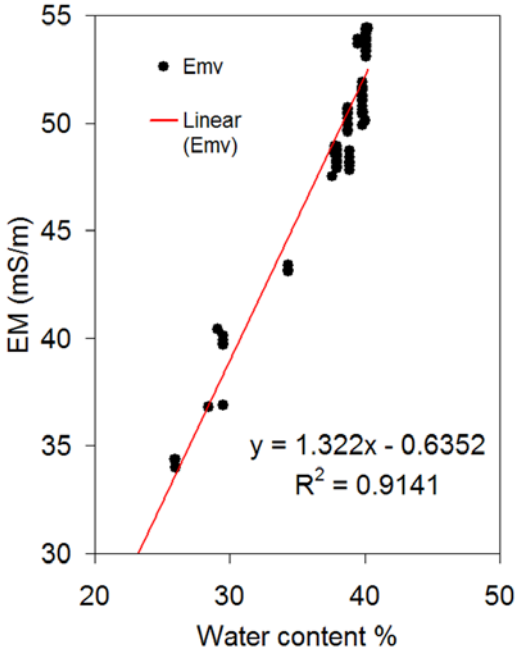

Figure 3. The EMI EC_a response as a function of soil water content during a drainage experiment. The water content was measured using a ThetaProbe buried at 40 cm depth. A linear trend line is fitted to the data, indicating a strong dependence of EC_a on θ.

3.4. Statistical Analysis

3.4.1. Data QA/QC

[23] The preliminary data analysis included a data quality check and a data cleaning procedure. As the field computer records data every few seconds it is important to go through the data and remove any points where the instrument was stationary, for instance at the beginning or end. This is done quite simply by viewing the data as a time series and checking the data against the GPS speed and removing values of 0 m s^{-1} and the low values surrounding them. The second check examines the magnitude of the EC_a response, any negative values are removed and the surrounding data points checked for consistency with previous data points. Metal watering cans used for irrigation can cause negative and positive anomalies in the EMI response. These were easily removed by plotting the data as a time series and picking out the characteristic blips.

3.4.2. Mapping Data Using a Block Kriging Procedure

[24] Once the data were processed, analysis of data mean, variance, and distribution were conducted. The assumption with kriging is that of a multi-Gaussian or normally distributed input data set. This can be achieved by transforming the data using a normal score transform to obtain a normal distribution with a mean of 0 and a variance of 1 [*Goovaerts*, 1997]. We performed this using the analysis package SGEMS [*Remy*, 2005]. Variograms were fitted to the data and then block kriged on a 2 × 2 m grid using Vesper [*Walter et al.*, 2001], which allows the use of a nonuniform field boundary, and kriging using the local variogram. Finally the data were normal score back transformed using SGEMS to produce the final kriged EC_a maps.

3.4.3. Temporal or Rank Stability

[25] Statistical analysis of nine kriged EC_a maps were conducted using differencing and the temporal or rank stability procedure described by *Vachaud et al.* [1985]. In this procedure the difference Δ_{ij} of each individual observation S_{ij} to the average $\overline{S}_j$ for the respective sampling time j is calculated with

$$\Delta_{ij} = S_{ij} - \overline{S}_j \tag{1}$$

And the relative difference is calculated by

$$\delta_{ij} = \frac{\Delta_{ij}}{\overline{S}_j} \tag{2}$$

For each sampling location an average relative difference $\overline{\delta}_{ij}$ is calculated by

$$\overline{\delta}_{ij} = \frac{\sum_{j=1}^{9} \delta_{ij}}{9} \tag{3}$$

for the nine sampling campaigns as well as its standard deviation σ. In the present study, the relative differences are shown in a georeferenced manner [e.g., *Wendroth et al.*, 1999]. In this way, the relative magnitude of the variable and its variation is known with respect to the location within the field and with respect to the behavior of neighboring locations.

4. Results and Discussion

4.1. EMI Dependence on θ

[26] The dependence of EC_a on θ, measured using the EMI sensor, was demonstrated using a drainage experiment; the results are presented in Figure 3. The clay % at this location was 34% and the EC_e was 0.6 dS/m, typical of the irrigation water applied to the site from the abandoned oxbow lake. The results, measured over a period of 3 weeks, with a consistent soil temperature of 31°C show an almost linear dependence of EC_a on water content over this range of θ. The result is not a unique calibration for the whole field site, and thus water content cannot be determined, with certainty, from the EC_a map. The slope of the graph may alter with increasing EC_e, as will the intercept of the trend line, moving up or down depending on the clay % or EC_e. The use of a linear trend line indicates a negative intercept, this occurs because the calibration would become increasingly nonlinear as the soil dried further [*Mualem and Friedman*, 1991]. Clearly, the data presented indicates a strong dependence of EC_a on θ during drainage.

4.2. Spatial Correlation

[27] The normal score semivariograms (Figure 4) demonstrate strong spatial correlation (data for all 9 semivariograms are presented). Double spherical semivariograms were fitted to the data in order to capture the strong correlation at less than 20 m. The nugget and range of the variograms (Table 1) indicate that the nugget is higher, and the range shorter, when the soil is dry. For the driest soil on 15 March the range is about 10 m, increasing to about 20 m when the soil is at its wettest. This is similar to the pattern

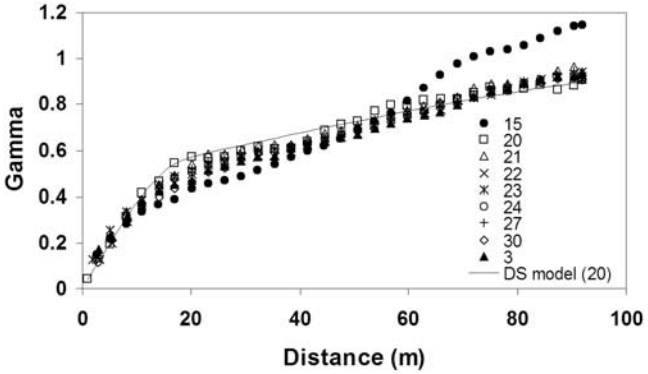

Figure 4. Semivariograms for the normal score EC_a data. All variograms are fitted with double spherical models. The numbers on the legend indicate the corresponding date in March or April 2007.

observed for θ measurements made in small watersheds, where the pattern becomes more random (disconnected) when the soil is dry [*Western et al.*, 1999].

[28] Four of the resulting kriged maps are presented in Figure 5. The locations with higher EC_a values are shown in dark red (>70 mS/m), the lowest EC_a values are shown in dark blue (<20 mS/m). On 15 March (M-15) the northern end of the field had the lowest EC_a values and the southwestern side had the highest. The 21 March (M-21) map follows a day after the 75 mm rainfall on the evening of 19–20 March (M-19/M20). Most of the blue zone (<30 mS/m) disappears, and the area in red (>70 mS/m) dramatically increases. This pattern persists through the end of March, and slowly the dark blue areas in the northern end of the field begin to reappear by 3 April (A-3).

[29] EC_a values for the different days can be compared after the completion of kriging. EC_a is strongly dependent on θ, demonstrated in Figure 3 and through the changes in Figure 6. The histograms (Figure 6) indicate that the EC_a does not reach a maximum until M-21, a couple of days after rainfall. The red and black lines indicate the general extremities of the observed data and demonstrate that the shape of the histograms change from being positively skewed when the soil is dry (red) to negatively skewed when the soil is wet (black). Noticeably, the soil does not reach its highest values of EC_a immediately following wetting. The maximum values are reached 4–5 days following the wetting. This suggests that it takes more time for the water to penetrate into the fine textured soil which continues to increase in EC_a over the 5 days following the rainfall. By A-3 (blue), 16 days later, the soil reached an intermediate stage between wet and dry.

[30] This interpretation is supported by the spearman rank correlation coefficients for the kriged data (Table 2). They show a lag in the EC_a response with the highest correlation occurring on M-21. The fact that the correlations are high before and immediately after rainfall, indicates a step increase in EC_a with the increase in water content. However, following the peak EC_a on M-21 the correlation begins to decline, as the time increases from the initial event and water redistributes in the subsurface. By the end of March/early April the correlation with M-15 begins to increase, as the soil dries, returning to similar conditions prior to wetting.

4.3. Difference Mapping and Temporal Stability

[31] The data collection on multiple days allows the data to be presented as a series of differenced time-lapse images. In Figure 7 the eight maps following the rainfall are compared to the map for dry soil (M-15) by subtracting it from the respective day. In this way we identify zones where the EC_a is higher (in red) and zones where the EC_a is the same or lower (in blue). Clearly, we can see the emergence of a zone with higher EC_a along the southeast edge of the field, which grows in size up to M-24 and dissipates thereafter. By A-3 three quarters of the field has returned to values similar to those found on M-15. However, the southeast portion of the field remains consistently higher than before. The dark blue areas that occur at the edges of the field (0 to −10 mS/m) in the difference map indicate locations where the EC_a decreased. This most likely occurred because of some leaching of ions in the days immediately after rainfall. Most of these locations at the edges of the field are close to water, either in the drainage channels or ponds, and thus evapoconcentration can occur at these edges resulting in soluble salt build up, which is quickly washed away by the rainfall.

[32] The temporal stability analysis of the nine maps provides us with an alternative way of looking at the data (Figure 8). Hand dug irrigation ponds (marked by circles on Figure 8), about 2 × 2 m and 1 m deep, are filled every few days with water from the abandoned oxbow lakes. The red dots indicate soil sampling locations and the three numbers associated with each sampling point indicate clay %, θ, and EC_e.

[33] The temporal stability varies by as much as 25 mS m^{-1} on either side of the field average EC_a. The red areas indicate locations that are consistently higher than the field average. The areas in blue show the locations that are consistently lower than the field average. We interpret this map to indicate a general transition in soil texture across the field with a combined increase in EC_e and clay % at the southern end of the field which acts almost as a sump. Clay percentages in the blue area tend to be in the low 30s, in the

Table 1. Variogram Range for the Double Spherical Fitted Variogram[a]

	15 Mar	20 Mar	21 Mar	22 Mar	23 Mar	24 Mar	27 Mar	30 Mar	3 Apr
Nugget	0.07	0.00	0.06	0.02	0.06	0.02	0.05	0.04	0.07
Short range	10.9	20.0	21.0	17.3	17.3	19.1	20.0	18.2	14.5
Long range	127.6	151.1	156.6	130.9	158.5	145.6	138.3	140.1	165.5

[a]Range is in meters.

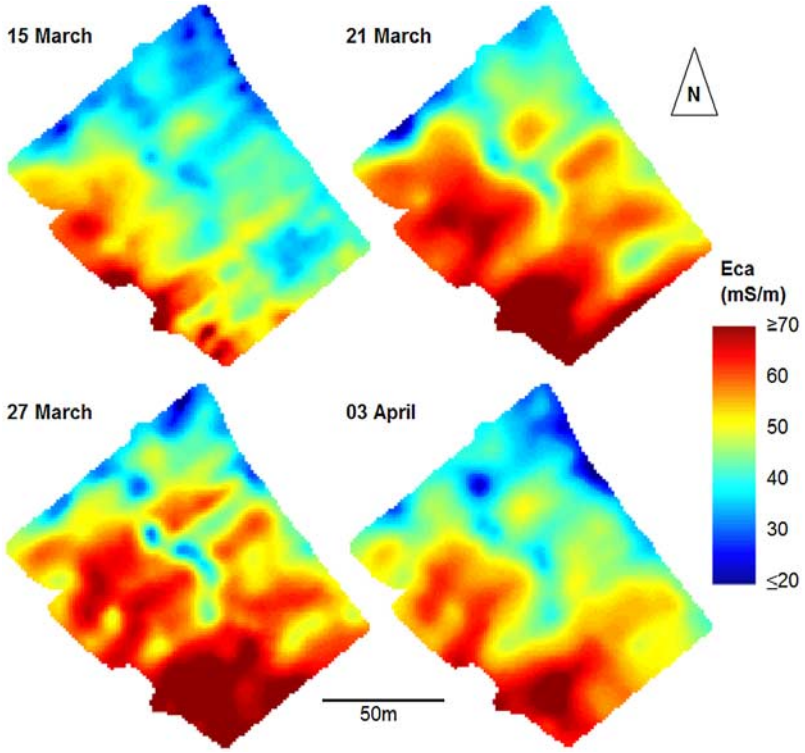

Figure 5. Kriged EC_a maps from four points in time; 15 March is before the rain, and the subsequent maps follow the increase and subsidence of the EC_a values following the rainfall event.

red areas these values increase into the 40s. The change in water content across the field is also consistent with this perceived textural variation, being lower in the blue areas and higher in the red areas.

[34] The standard deviation of the temporal stability map presented in Figure 8b shows strong patterns. The locations of greatest change are associated with particular features of the field, such as the irrigation ponds in the center of the field, which also represent the perceived watershed in the field. Notice that the red patch near the black triangle, indicating the location of a ponded infiltration experiment, migrates to the NE (black arrow). This indicates that with the addition of so much water a lot of it went laterally. In contrast the two irrigation ponds toward the southern end of the field migrate to the NE and SW, either side of the perceived watershed. Red patches also occur at the locations where the irrigation water is pumped from the oxbow, where

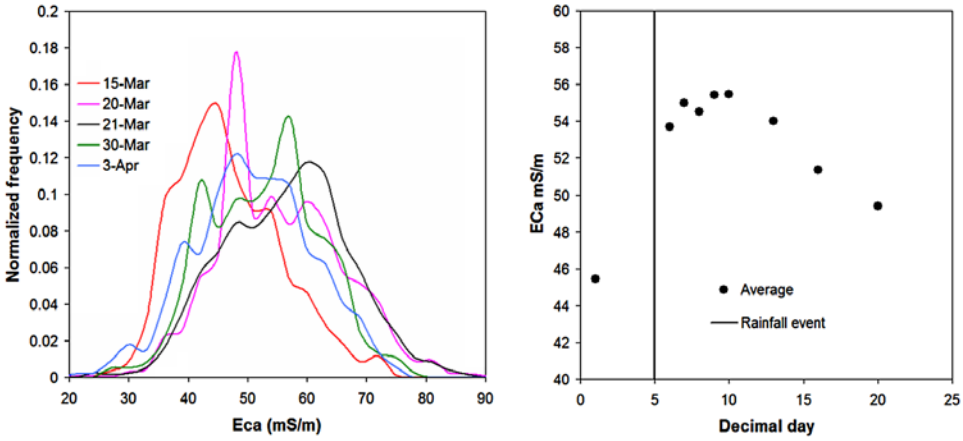

Figure 6. (left) EC_a is assumed to be dependent on the water content. The lines show the EC_a distribution from the kriged map values as the soil wets and dries. The red line shows when the soil was at its driest, and the black line shows the soil as it reaches its maximum average EC_a value. (right) The average EC_a as a function of time, indicating that after 3 weeks of dry weather the EC_a (water content) has not entirely recovered the prerainfall value.

Table 2. Spearman Rank Correlation Coefficient for the Maps of Kriged Data for the Different Mapping Days

	15 Mar	21 Mar	21 Mar	22 Mar	23 Mar	24 Mar	27 Mar	30 Mar	3 Apr
15 Mar	1.000								
20 Mar	0.819	1.000							
21 Mar	0.833	0.988	1.000						
22 Mar	0.811	0.953	0.950	1.000					
23 Mar	0.671	0.880	0.876	0.908	1.000				
24 Mar	0.670	0.889	0.882	0.914	0.994	1.000			
27 Mar	0.741	0.854	0.860	0.874	0.855	0.854	1.000		
30 Mar	0.754	0.853	0.871	0.870	0.850	0.847	0.989	1.000	
3 Apr	0.700	0.836	0.857	0.846	0.876	0.874	0.914	0.924	1.000

the pumps leak water leaching the soil, and at the edges of the drainage channel at the northern end of the field.

4.4. Soil and Surface Water Sample Data

[35] In addition to the geophysical imaging, soil samples from the locations indicated on the map in Figure 8a were analyzed for clay %, EC_e and θ (Table 3). Given a snapshot sample, and varying texture and EC_e across a field, clay % and EC_e were expected to give the higher correlation with the EC_a signal. Although EC_a is strongly dependent on θ (Figure 3), the sampling on a single day, at a point in time, does not capture the temporal change in θ given different texture-dependent calibrations. Multiple linear regression indicated EC_e as more significant than clay %. Simple linear regression of each individual variable gave an r^2 of 0.68 for EC_e, 0.44 for clay % and 0.24 for θ. This indicates that EC_e and clay % dominate the signal response. Surface water measurements from the oxbows and from flood irrigated plots at the south of the field also indicated a strong increase in surface water EC toward the southern end of the field (Figure 9b). This is consistent with this location acting as a drainage sump. The highest surface water value of 242 mS/m (2.42 dS/m) was found in one of the flood irrigated plots and was considered to be high because of evapoconcentration. Water in the oxbow to the NE generally had EC values ~40 mS/m, 6 times lower. The areas with increased surface water EC were also consistent with higher pH values. pH values increased to ~8, close to the equilibrium value with calcium carbonate (Figure 9c), calcium being the dominant cation in the surface waters.

4.5. Geochemical Interpretation of EMI Maps and Preliminary Arsenic Sample Data

[36] A range of questions were posed in the introduction with regard to assisting the biogeochemist to interpret the soil processes at the field scale. In any biogeochemical study where point samples are made, the question remains as to whether the sampling locations are representative of that general location. The novel approach presented in this work has been to measure the spatiotemporal response of soil EC_a as a surrogate for monitoring soil hydrological processes during drainage. The first question, "in which area of the field site is change in conditions most apparent?," can be answered by Figure 8b, where we identify locations with large standard deviations, indicating that the EC_a response is most variable in these locations. The

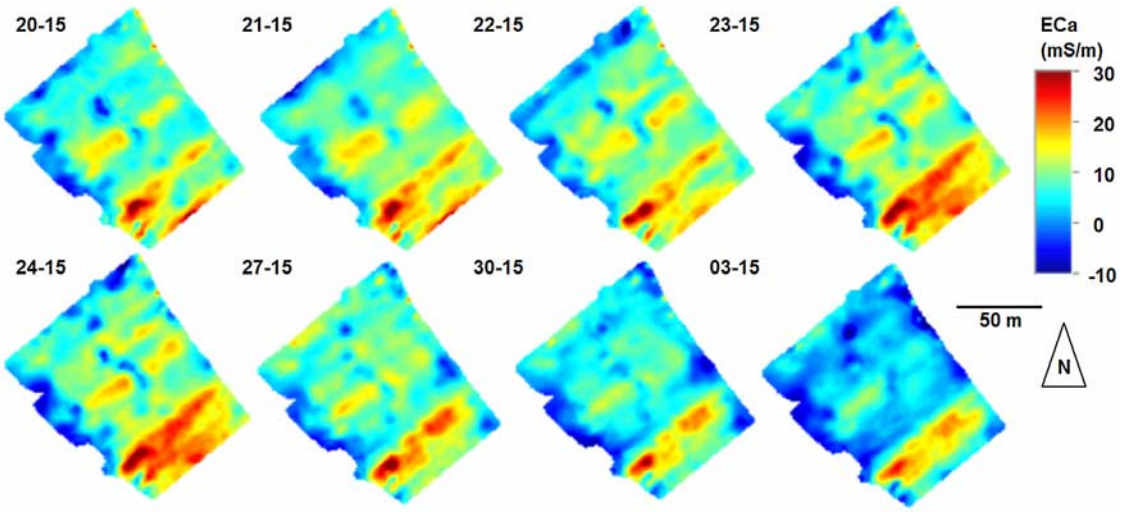

Figure 7. Time-lapse EC_a difference maps, where the map collected before the rain is subtracted from each map after the rain. In this way locations that are higher or lower than the EC_a values prior to rainfall can be determined. The red zones indicate EC_a values considerably higher than before the rain. Note the rise in EC_a in the SW end of the field.

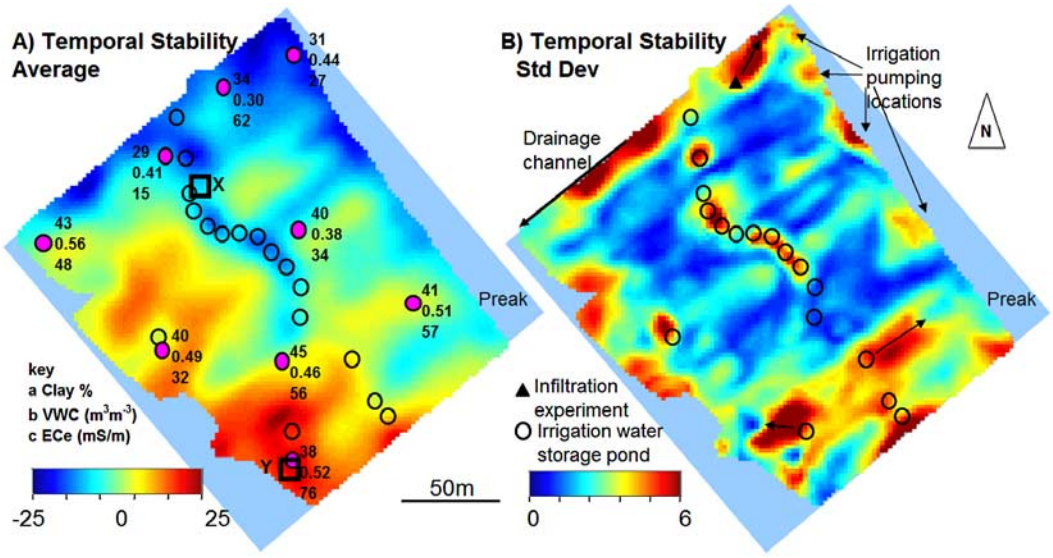

Figure 8. (a) The temporal stability map of the nine maps. The red areas depict locations where the EC_a is consistently higher than the field average, and the blue areas depict locations where the EC_a is consistently lower than the field average. (b) The standard deviation of the temporal stability map. The red areas indicate the locations undergoing the most change. These locations are clearly associated with the ponds that are wet and dry on a regular basis. Locations X and Y correspond to two nested well sampling locations for arsenic.

greatest variability is associated with the irrigation ponds, consistently drained and refilled with water, and the edges of the field site where water moves into field drains. The second question, "in which part of the field site does water drain more rapidly, and following a precipitation event which locations return to prerainfall conditions most quickly, and how long does this take?," can be inferred from Figure 7. This is based on the assumption that as the θ increases so the difference between wet and dry EC_a increases. As the soil drains the EC_a is expected to return to a value close to the antecedent EC_a when the soil was dry. It can be seen that the coarse textured soils in the northern end of the field return to their previous values most rapidly, turning from yellow to pale blue, the mid section of the field has returned to its previous state by April, but the southern end of the field remains well above its initial state by April, though showing a general decline. The answer to the question, "where is the soil most likely to be wettest the longest?," is toward the southern end of the field. Observation confirmed this as the northern end of the field was unsaturated in the top 30 cm of soil by April but soil at the southern end remained saturated. Answering the question "where are the locations where clay is most likely to have accumulated?" is never easy. The traditional soil survey approach would be to use features in the landscape, color and texture samples to try and delineate this. The EMI map provides an extra layer of information in a landscape largely devoid of topographic difference or clear soil boundaries. Combining the EMI map and the texture sample locations indicates a general increase in the clay % trending from the northern end of the field site to the south. This makes some sense in that the southern end is covered by water for the longest period, as evidenced by the north–south crop transition from vegetables and herbs at the northern end of the field to rice at the southern end. This means that at the northern end there is less time for the fine clays to settle from the flood waters, there being more time for this to occur at the southern end. The build up of soluble salts also

Table 3. Data Corresponding to the Sampling Sites Shown in Figure 7[a]

EMI_v	EMI_h	EMI_h/EMI_v	EMI_v/EC_e	Clay %	VWC	EC_e (mS/m)	pH
31.5	18.1	0.57	1.2	31	0.44	27	7.10
52.7	47.1	0.89	0.9	34	0.30	62	NA
36.6	21.6	0.59	2.4	29	0.41	15	6.90
39.2	26.2	0.67	1.2	40	0.38	34	6.77
58.5	43.4	0.74	1.2	43	0.56	48	7.07
53.4	36.5	0.68	0.9	41	0.51	57	6.65
53.8	38.1	0.79	2.3	40	0.49	32	6.95
56.0	41.8	0.75	1.0	45	0.46	56	6.55
64.2	45.9	0.71	0.9	38	0.52	76	6.86

[a]Data are shown from top to bottom and from left to right. Electromagnetic induction (EMI) values are given in mS/m, and VWC is given in $m^3\ m^{-3}$. EMI_v is vertical induction, and EMI_h is horizontal induction.

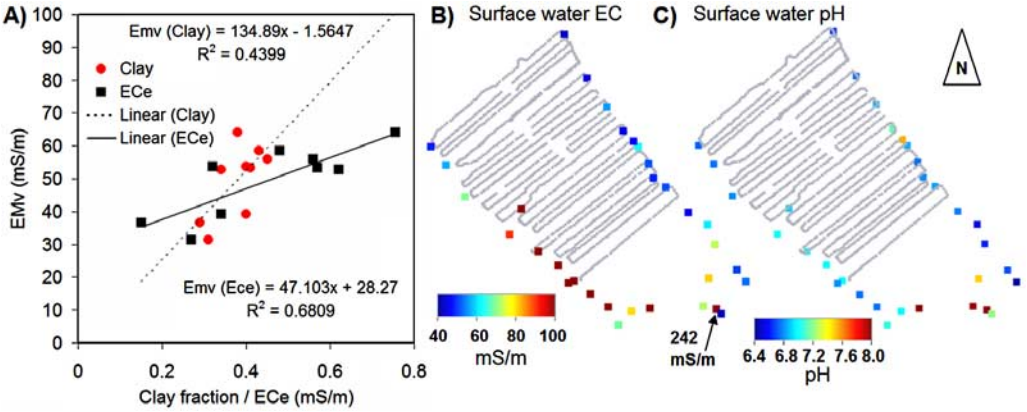

Figure 9. (a) EMv as a function of the clay fraction and the EC_e, the two significant variables found to impact the EMv value. (b) The electrical conductivity of the surface water at 10 cm depth corrected to a value at 25°C and (c) the pH at the same locations.

appears to follow this general north–south trend with the higher levels toward the southern end of the fields. The longer periods of soil saturation facilitate greater evapoconcentration. We tested the surface water as it transitions from the abandoned oxbow lakes to the flood irrigated fields. Figure 9b shows that the surface water in the flood irrigated fields at the southern end of the field site had EC values two to three times greater than the water in the oxbow lakes. The data provided by the combination of the EMI time-lapse imaging, and the soil samples provided the geochemical researchers with a unique spatiotemporal perspective on the hydrological and soil processes occurring on the field site.

[37] The information provided by the EMI imaging provided a geospatial data set to assist in locating contrasting sites for sampling [As]. EMI drastically improves the spatial (and temporal) coverage of an area when combined with other methods. The major contribution of the EMI method is to provide, with more confidence, areas of interest for direct sampling rather than replace the sampling methods (i.e., we cannot infer [As] concentrations, but on the basis of the EMI data we can propose areas that might be of interest). Total [As] concentration data from 2 nested well locations [*Kocar et al.*, 2008] are indicated in Figure 8a by the black squares marked by X and Y. X is toward the low-EC_a region of the field and Y is in the high-EC_a region of the field. The results from the EMI survey assisted in locating the second nested well location (X, Figure 8a) to contrast with the existing nested well location at Y. X was located as far into the northern end of the field site as the constraints (landowners permission) would allow. The hypothesis being tested by the biogeochemistry research team was that changes in soil redox conditions, due to annual wetting and drying cycles, leads to the desorption of [As] from the solids into the pore water. The onset of reducing conditions and ensuing reductive dissolution of As-bearing Fe (hydr)oxides leads to the mobilization of [As] from soil particles into the soil solution [*Polizzotto et al.*, 2008; *Polizzotto et al.*, 2005]. As a result the biochemists were trying to identify locations where clay %, EC_e and θ were higher for longer periods. The implication being that these locations would act as a better source for [As] that might steadily migrate further down into the sediment, thus leading to higher observable concentrations under these locations. Recent work suggests that this is a reasonable assumption, with higher EMI signal responses having shown correlation to locations with [As] in groundwater during research in Bangladesh [*Aziz et al.*, 2008]. Our research makes no attempt to answer the question of whether this hypothesis is true, but simply assisted in identifying areas that contrasted in their hydrological behavior (wet and dry).

[38] Preliminary [As] concentration values from the two nested well locations did differ noticeably with increasing depth (Figure 10). The values at the southern Y location was consistently higher than at the northern location, X. The EMI images proved valuable and are encouraging, indicating that valuable insight can be obtained for interdisciplinary studies. Further research should be conducted over a wider area to determine if any observable relationship exists between the geophysical signal (EC_a) and [As] concentration found in sediments in this area. Regardless of the processes governing the release of [As] into aquifers, establishing an empirical link between a geophysical signal and [As] concentrations in sediment pore waters could prove immensely helpful in improving the sighting of drinking water wells from the humanitarian perspective.

5. Conclusions

[39] We demonstrate that EMI can provide a rapid, campaign-style imaging method that does not need to be left in situ but still provides invaluable insight into subsurface hydrological processes. We present a sequence of EMI time series geophysical images of a 4 ha deltaic field site. The spatiotemporal images are used to interpret soil hydrological processes in a tropical deltaic landscape, devoid of topographic features that could assist in interpreting soil hydrological behavior. The imaging was conducted before and after a rainfall event and the subsequent natural drainage and redistribution. Data is interpreted using differencing in time and using rank stability analysis to identify contrasting locations where the most substantial change occurs

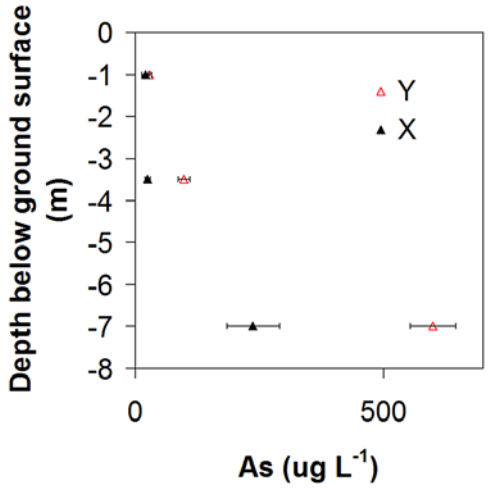

Figure 10. Total [As] concentration from nested well locations at sites X and Y corresponding to those shown in Figure 8. The data indicate a much higher arsenic concentration in the location corresponding to high EC_a values.

in the geophysical response. The imaging provides qualitative visual insight into the hydrological redistribution processes occurring within the soils of the field site. The novel methodology is particularly suited to campaign style field work in developing countries, where time and data acquisition security are major issues. We identify zones which exhibit the most ''change,'' these are interpreted as locations consistent with soil moisture depletion, or locations from where water appears to drain and leach salts. The southern end of our 4 ha field site shows behavior consistent with a drainage sump, and liable to enhanced solution EC due to evapoconcentration. This interpretation is consistent with EC values measured from surface water and with the cropping patterns in the location. The EMI data was used to assist in locating a second nested well site so that it showed the most contrast between the soil EC_a data. [As] concentrations from the well data from the two locations showed increasing divergence with depth, the controlling processes are not explained, but the new imaging approach shows good potential for assisting biogeochemical researchers in assessing the spatiotemporal characteristics of a field site from which they collect point samples.

[40] **Acknowledgments.** We are grateful to A. Falen at the University of Idaho Pedology Lab for textural analysis. We would like to also acknowledge all those who assisted in this work in Cambodia as Cambodia Resource Development International (RDIC).

References

Abdu, H., D. A. Robinson, and S. B. Jones (2007), Comparing bulk soil electrical conductivity determination using the DUALEM-1S and EM38-DD electromagnetic induction instruments, *Soil Sci. Soc. Am. J.*, *71*, 189–196.

Ahmed, K. M., P. Bhattacharya, M. A. Hasan, S. H. Akhter, S. M. M. Alam, M. A. H. Bhuyian, M. B. Imam, A. A. Khan, and O. Sracek (2004), Arsenic enrichment in groundwater of the alluvial aquifers in Bangladesh: An overview, *Appl. Geochem.*, *19*, 181–200, doi:10.1016/j.apgeochem.2003.09.006.

Ahmed, M. F., S. Ahuja, M. Alauddin, S. J. Hug, J. R. Lloyd, A. Pfaff, T. Pichler, C. Saltikov, M. Stute, and A. van Geen (2006), Epidemiology: Ensuring safe drinking water in Bangladesh, *Science*, *314*, 1687–1688, doi:10.1126/science.1133146.

Aziz, Z., et al. (2008), Impact of local recharge on arsenic concentrations in shallow aquifers inferred from the electromagnetic conductivity of soils in Araihazar, Bangladesh, *Water Resour. Res.*, *44*, W07416, doi:10.1029/2007WR006000.

Benner, S. G., M. L. Polizzotto, B. D. Kocar, M. Sampson, and S. Fendorf (2008), Groundwater flow in an arsenic-contaminated aquifer, Mekong delta, Cambodia, *Appl. Geochem.*, *23*, 3072–3087.

Beven, K. J. (2001), *Rainfall-Runoff Modelling: The Primer*, John Willey, Chichester, U. K.

Bourgault, G., A. G. Journel, J. D. Rhoades, D. L. Corwin, and S. M. Lesch (1997), Geostatistical analysis of a soil salinity data set, *Adv. Agron.*, *58*, 241–292, doi:10.1016/S0065-2113(08)60257-6.

Callegary, J. B., T. P. A. Ferre, and R. W. Groom (2007), Spatial sensitivity of low-induction-number frequency-domain electromagnetic induction instruments, *Vadose Zone J.*, *6*, 158–167, doi:10.2136/vzj2006.0120.

Clark, I., and P. Fritz (1997), *Environmental Isotopes in Hydrogeology*, CRC Press, Boca Raton, Fla.

Comas, X., L. Slater, and A. Reeve (2004), Geophysical evidence for peat basin morphology and stratigraphic controls on vegetation observed in a northern peatland, *J. Hydrol.*, *295*, 173–184, doi:10.1016/j.jhydrol.2004.03.008.

Corwin, D. L., and S. M. Lesch (2003), Application of soil electrical conductivity to precision agriculture: Theory, principles, and guidelines, *Agron. J.*, *95*, 455–471.

Corwin, D. L., and S. M. Lesch (2005), Characterizing soil spatial variability with apparent soil electrical conductivity: I. Survey protocols, *Comput. Electron. Agric.*, *46*, 103–133, doi:10.1016/j.compag.2004.11.002.

Daly, E., and A. Porporato (2005), A review of soil moisture dynamics: From rainfall infiltration to ecosystem response, *Environ. Eng. Sci.*, *22*, 9–24, doi:10.1089/ees.2005.22.9.

deLemos, J. L., B. C. Bostick, C. E. Renshaw, S. Sturup, and X. H. Feng (2006), Landfill-stimulated iron reduction and arsenic release at the Coakley Superfund site (NH), *Environ. Sci. Technol.*, *40*, 67–73, doi:10.1021/es051054h.

Doolittle, J. A., K. A. Sudduth, N. R. Kitchen, and S. J. Indorante (1994), Estimating depths to claypans using electromagnetic induction methods, *J. Soil Water Conserv.*, *49*, 572–575.

Flury, M., and N. N. Wai (2003), Dyes as tracers for vadose zone hydrology, *Rev. Geophys.*, *41*(1), 1002, doi:10.1029/2001RG000109.

Friedman, S. P. (2005), Soil properties influencing apparent electrical conductivity: A review, *Comput. Electron. Agric.*, *46*, 45–70, doi:10.1016/j.compag.2004.11.001.

Gee, G. W., and J. W. Bauder (1986), Particle-size analysis, in *Methods of Soil Analysis Part 1: Physical and Mineralogical Methods*, *Soil Sci. Soc. Am. Book Ser.*, vol. 5, 2nd ed., edited by A. Klute, pp. 383–411, Am. Soc. of Agron., Madison, Wis.

Goovaerts, P. (1997), *Geostatistics for Natural Resources Evaluation*, Oxford Univ. Press, New York.

Harvey, C. F., et al. (2002), Arsenic mobility and groundwater extraction in Bangladesh, *Science*, *298*, 1602–1606, doi:10.1126/science.1076978.

Hendrickx, J. M. H., and R. G. Kachanoski (2002), Nonintrusive electromagnetic induction, in *Methods of Soil Analysis. Part 1*, edited by J. Dane and C. Topp, pp. 1301–1310, Soil Sci. Soc. of Am., Madison, Wis.

Hendrickx, J. M. H., B. Baerends, Z. I. Raza, M. Sadiq, and M. A. Chaudhry (1992), Soil salinity assessment by electromagnetic induction on irrigated land, *Soil Sci. Soc. Am. J.*, *56*, 1933–1941.

Huisman, J. A., S. S. Hubbard, J. D. Redman, and A. P. Annan (2003), Measuring soil water content with ground penetrating radar: A review, *Vadose Zone J.*, *2*, 476–491.

James, I. T., T. W. Waine, R. I. Bradley, J. C. Taylor, and R. J. Godwin (2003), Determination of soil type boundaries using electromagnetic induction scanning techniques, *Biosyst. Eng.*, *86*, 421–430, doi:10.1016/j.biosystemseng.2003.09.001.

Jung, W. K., N. R. Kitchen, K. A. Sudduth, R. J. Kremer, and P. P. Motavalli (2005), Relationship of apparent soil electrical conductivity to claypan soil properties, *Soil Sci. Soc. Am. J.*, *69*, 883–892, doi:10.2136/sssaj2004.0202.

Kachanoski, R. G., E. G. Gregorich, and I. J. Van Wesenbeeck (1988), Estimating spatial variations of soil water content using non-contacting electromagnetic inductive methods, *Can. J. Soil Sci.*, *68*, 715–722.

Kachanoski, R. G., E. De Jong, and J. M. H. Hendrickx (2002), Nonintrusive water content measurement in the field, in *Methods of Soil Analysis. Part 1*, edited by J. Dane and C. Topp, pp. 497–501, Soil Sci. Soc. of Am., Madison, Wis.

Knight, R. (2001), Ground penetrating radar for environmental applications, *Annu. Rev. Earth Planet. Sci.*, *29*, 229–255, doi:10.1146/annurev.earth.29.1.229.

Kocar, B. D., M. L. Polizzotto, S. G. Benner, S. M. Ying, M. Ung, K. Ouch, M. Sampson, and S. Fendorf (2008), Integrated biogeochemical and hydrologic processes driving arsenic release from shallow sediments to groundwaters of the Mekong delta, *Appl. Geochem.*, *23*, 3059–3071.

Lane, S. N., C. J. Brookes, M. J. Kirkby, and J. Holden (2004), A network-index-based version of TOPMODEL for use with high-resolution digital topographic data, *Hydrol. Processes*, *18*, 191–201, doi:10.1002/hyp.5208.

Lesch, S. M., D. J. Strauss, and J. D. Rhoades (1995a), Spatial prediction of soil salinity using electromagnetic induction techniques: 2. An efficient spatial sampling algorithm suitable for multiple linear regression model identification and estimation, *Water Resour. Res.*, *31*, 387–398, doi:10.1029/94WR02180.

Lesch, S. M., D. J. Strauss, and J. D. Rhoades (1995b), Spatial prediction of soil salinity using electromagnetic induction techniques: 1. Statistical prediction models: A comparison of multiple linear regression and cokriging, *Water Resour. Res.*, *31*, 373–386, doi:10.1029/94WR02179.

Looms, M. C., H. K. H. Jensena, A. Binley, and L. Nielsena (2008), Monitoring unsaturated flow and transport using cross-borehole geophysical methods, *Vadose Zone J.*, *7*, 227–237, doi:10.2136/vzj2006.0129.

McArthur, J. M., P. Ravenscroft, S. Safiulla, and M. F. Thirlwall (2001), Arsenic in groundwater: Testing pollution mechanisms for sedimentary aquifers in Bangladesh, *Water Resour. Res.*, *37*, 109–117, doi:10.1029/2000WR900270.

McNeill, J. D. (1980), Electromagnetic terrain conductivity measurement at low induction numbers, *Tech Note TN-6*, Geonics, Mississauga, Ont., Canada.

Mualem, Y., and S. P. Friedman (1991), Theoretical prediction of electrical-conductivity in saturated and unsaturated soil, *Water Resour. Res.*, *27*, 2771–2777, doi:10.1029/91WR01095.

Nettleton, W. D., L. Bushue, J. A. Doolittle, T. J. Endres, and S. J. Indorante (1994), Sodium-affected soil identification in south-central Illinois by electromagnetic induction, *Soil Sci. Soc. Am. J.*, *58*, 1190–1193.

Nguyen, V. L., T. K. O. Ta, and M. Tateishi (2000), Late Holocene depositional environments and coastal evolution of the Mekong River Delta, southern Vietnam, *J. Asian Earth Sci.*, *18*, 427–439, doi:10.1016/S1367-9120(99)00076-0.

Noborio, K., K. J. Mclnnes, and J. L. Heilman (1996), Measurements of cumulative infiltration and wetting front location by time domain reflectometry, *Soil Sci.*, *161*, 480–483, doi:10.1097/00010694-199608000-00002.

Philip, J. R. (1969), Theory of infiltration, *Adv. Hydrosci.*, *5*, 215–296.

Polizzotto, M. L., C. F. Harvey, S. R. Sutton, and S. Fendorf (2005), Processes conducive to the release and transport of arsenic into aquifers of Bangladesh, *Proc. Natl. Acad. Sci. U. S. A.*, *102*, 18,819–18,823, doi:10.1073/pnas.0509539103.

Polizzotto, M. L., B. D. Kocar, S. G. Benner, M. Sampson, and S. Fendorf (2008), Near-surface wetland sediments as a source of arsenic release to ground water in Asia, *Nature*, *454*, 505–508, doi:10.1038/nature07093.

Remy, N. (2005), S-GEMS: The Stanford geostatistical modeling software: A tool for new algorithms development, *Geostatistics Banff 2004: 7th International Geostatistics Conference, Quantitative Geology and Geostatistics*, vol. 1, edited by O. Leuangthong and C. V. Deutsch, pp. 865–871, Springer, New York.

Rhoades, J. D. (1982), Soluble salts, in *Methods of Soil Analysis: Part 2: Chemical and Microbiological Properties*, *Monogr. 9*, 2nd ed., edited by A. L. Page et al., pp. 149–157, Am. Soc. Agron., Madison, Wis.

Robinson, D. A., C. S. Campbell, J. W. Hopmans, B. K. Hornbuckle, S. B. Jones, R. Knight, F. Ogden, J. Selker, and O. Wendroth (2008a), Soil moisture measurement for ecological and hydrological watershed scale observatories: A review, *Vadose Zone J.*, *7*, 358–389, doi:10.2136/vzj2007.0143.

Robinson, D. A., et al. (2008b), Advancing process-based watershed hydrological research using near-surface geophysics: A vision for, and review of, electrical and magnetic geophysical methods, *Hydrol. Processes*, *22*, 3604–3635, doi:10.1002/hyp.6963.

Robinson, D. A., H. Abdu, S. B. Jones, M. Seyfried, I. Lebron, and R. Knight (2008c), Eco-geophysical imaging of watershed-scale soil patterns links with plant community spatial patterns, *Vadose Zone J.*, *7*, 1132–1138.

Rubin, Y., and S. S. Hubbard (2005), *Hydrogeophysics*, 523 pp., Springer, New York.

Sheets, K. R., and J. M. H. Hendrickx (1995), Noninvasive soil water content measurement using electromagnetic induction, *Water Resour. Res.*, *31*, 2401–2409, doi:10.1029/95WR01949.

Sherlock, M. D., and J. J. McDonnell (2003), A new tool for hillslope hydrologists: Spatially distributed groundwater level and soil water content measured using electromagnetic induction, *Hydrol. Processes*, *17*, 1965–1977, doi:10.1002/hyp.1221.

Si, B. C., and R. G. Kachanoski (2000), Unified solution for infiltration and drainage with hysteresis: Theory and field test, *Soil Sci. Soc. Am. J.*, *64*, 30–36.

Ta, T. K. O., V. L. Nguyen, M. Tateishi, I. Kobayashi, S. Tanabe, and Y. Saito (2002), Holocene delta evolution and sediment discharge of the Mekong River southern Vietnam, *Quat. Sci. Rev.*, *21*, 1807–1819, doi:10.1016/S0277-3791(02)00007-0.

Triantafilis, J., and S. M. Lesch (2005), Mapping clay content variation using electromagnetic induction techniques, *Comput. Electron. Agric.*, *46*, 203–237, doi:10.1016/j.compag.2004.11.006.

Vachaud, G., A. Passerat de Silans, P. Balabanis, and M. Vauclin (1985), Temporal stability of spatially measured soil water probability density function, *Soil Sci. Soc. Am. J.*, *49*, 822–828.

Walter, C., A. B. McBratney, A. Douaoui, and B. Minasny (2001), Spatial prediction of topsoil salinity in the Chelif valley, Algeria, using local kriging with local variograms versus local kriging with whole-area variogram, *Aust. J. Soil Res.*, *39*, 259–272, doi:10.1071/SR99114.

Wendroth, O., W. Pohl, S. Koszinski, H. Rogasik, C. J. Ritsema, and D. R. Nielsen (1999), Spatio-temporal patterns and covariance structures of soil water status in two northeast-German field sites, *J. Hydrol.*, *215*, 38–58, doi:10.1016/S0022-1694(98)00260-1.

Western, A. W., R. B. Grayson, G. Blöschl, G. R. Willgoose, and T. A. McMahon (1999), Observed spatial organization of soil moisture and its relation to terrain indices, *Water Resour. Res.*, *35*, 797–810, doi:10.1029/1998WR900065.

Western, A. W., R. B. Grayson, and G. Blöschl (2002), Scaling of soil moisture: A hydrologic perspective, *Annu. Rev. Earth Planet. Sci.*, *30*, 149–180, doi:10.1146/annurev.earth.30.091201.140434.

N. Crook, Department of Geophysics, Stanford University, Stanford, CA 94305, USA.

S. Fendorf and B. Kocar, Department of Environmental Earth System Science, Stanford University, Stanford, CA 94305, USA.

I. Lebron and D. A. Robinson, Department of Food Production, University of the West Indies, Saint Augustine, Trinidad and Tobago. (darearthscience@yahoo.com)

K. Phan and M. Sampson, Resource Development International Cambodia, P.O. Box 494, Phnom Penh, Cambodia.